Available online at www.sciencedirect.com
ScienceDirect
Comput. Methods Appl. Mech. Engrg. 196 (2006) 502–515
Computer methods in applied mechanics and engineering
www.elsevier.com/locate/cma

Development of a continuity-preserving segregated method for incompressible Navier–Stokes equations

Tony W.H. Sheu [a,*], R.K. Lin [a,1], G.L. Liu [b]

[a] *Department of Engineering Science and Ocean Engineering, National Taiwan University, No. 1, Sec. 4, Roosevelt Road, 106 Taipei, Taiwan, ROC*
[b] *Shanghai Institute of Applied Mathematics and Mechanics, Shanghai University, China*

Received 5 October 2004; received in revised form 5 October 2004; accepted 12 May 2006

Abstract

The present study aims to develop a new method for obtaining the non-oscillatory incompressible Navier–Stokes solutions on the non-staggered grids. Within the segregated grid framework, the divergence-free equation is chosen to replace one of the momentum equations so as to preserve the fluid incompressibility. For the sake of numerical accuracy, the five-point stencil convection–diffusion–reaction scheme is developed to obtain the nodally exact solution for this chosen momentum equation. The validity of the proposed mass-preserving Navier–Stokes method is justified by solving the three problems which are amenable to analytical solutions. The simulated solution quality is shown to outperform that of the conventional segregated approach, besides gaining a very high spatial rate of convergence.

Keywords: Incompressible; Segregated grid; Divergence-free equation; Convection–diffusion–reaction

1. Introduction

Simulation of the practically important incompressible fluid flow is academically difficult because analysis of this class of fluid flow governing equations is subjected to the divergence-free constraint condition and is susceptible to the numerical instability. As it is well known that the central approximation of advective terms tends to yield oscillations primarily in the velocity field. To eliminate this instability problem, one can apply advective schemes which accommodate the upwinding characteristics [1]. Another numerical instability problem mentioned frequently in the analysis of incompressible flow equations, cast in primitive variables, is manifested by showing two separate pressure solutions at the alternating nodes. In general, the SIMPLE algorithm [2], a frequently applied pressure-based method, is implemented on the staggered grid system to prevent the decoupling between the velocity and pressure. This grid system is, however, technically rather complicated for programming and requires a large amount of computer storage. The collocated grid system is therefore employed, in particular, for real-world applications. On the non-staggered (collocated) grids, the simulated oscillatory solutions are evident if the central differencing (or linear interpolation) is used to approximate the pressure gradient term in the momentum equations and the cell-face velocity in the continuity equation [3]. As a consequence, the end result is an oscillatory pressure field. For these reasons, we are motivated to eliminate the checkerboarding problem without resorting to staggered grid approaches. One of the most popular methods to prevent the decoupling of pressure and velocity in the co-located grid system is the Rhie–Chow interpolation method [4]. As the spatial dimension exceeds one, the numerical approximation of advective terms can give rise to false diffusion error [5]. Therefore, it is essential that the chosen flux discretization scheme should eliminate the cross-wind error without sacrificing the scheme stability.

* Corresponding author. Tel.: +886 2 33665791; fax: +886 2 23929885.
E-mail addresses: twhsheu@ntu.edu.tw (T.W.H. Sheu), rklin@ntu.edu.tw (R.K. Lin).
[1] Tel.: +886 2 33664429.

0045-7825/$ - see front matter
doi:10.1016/j.cma.2006.05.004

The need to suppress oscillations of different origins (velocity and pressure) without accuracy deterioration motivated the current study.

Another computational challenge in the simulation of incompressible Navier–Stokes equations is the enforcement of divergence-free constraint condition for the velocity field. One trivial way to preserve the mass conservation is to employ the mixed formulation for solving the equations of motion together with the incompressible constraint condition. The resulting coupled equations are, however, less diagonally dominant. In addition to the increased matrix size, the poor eigenvalue distribution makes the calculation of primitive variables much more difficult. To overcome the conventional difficulties encountered in the mixed formulation, the segregated algorithm has been proposed to separately solve the momentum equations for the velocity components and the Poisson equation for the pressure. In the literature, numerical methods developed within the PPE (pressure Poisson equation) framework [6] have been employed successfully in the simulation of incompressible Navier–Stokes equations. Slow convergence has, however, been frequently reported in the literature due to the negligence of the lower-order coupling terms [1]. For this reason, we are motivated to revisit the PPE method in a rigorous way.

The rest of this paper is organized as follows. In Section 2, the working equations in the primitive-variable description are solved subjected to the boundary conditions for the pressure Poisson equation. This is followed by presenting the currently developed segregated solution algorithm on non-staggered grids. In Section 4, the underlying convection–diffusion–reaction (CDR) scheme is employed to solve the momentum equations with the emphasis on its fundamental analysis. In Section 5, validation of the model is accomplished by solving problems which are all amenable to the analytical solutions. Finally, some conclusions are drawn in Section 6.

2. Working equations

In this study our attention is focused on the two-dimensional fluid flow governed by the following continuity equation and the Navier–Stokes equations, respectively:

$$\nabla \cdot \underline{\mathbf{u}} = 0, \tag{2.1}$$

$$\frac{\partial \underline{\mathbf{u}}}{\partial t} + (\underline{\mathbf{u}} \cdot \nabla)\underline{\mathbf{u}} = -\nabla p + \frac{1}{Re}\nabla^2 \underline{\mathbf{u}}. \tag{2.2}$$

For the purpose of closure, primitive variables $(\underline{\mathbf{u}}, p)$ are subjected to an initial divergence-free velocity field and the specified boundary velocity. All the lengths are scaled by L, the velocity components by u_∞, the time by L/u_∞ and the pressure by ρu_∞^2, where ρ denotes the fluid density. The Reynolds number $Re(\equiv \rho u_\infty L/\mu)$ is the consequence of the normalization of momentum equations.

Conservation of mass can be directly achieved by taking into account the divergence-free constraint equation (continuity equation). The eigenvalues of the resulting matrix equation become, however, increasingly ill-conditional and the incompressible flow solutions are very difficult to obtain. Besides this disadvantage, the required peripheral storage for the system of matrix equations may exceed the available computer power and disk space. Such a drawback discourages the use of coupled formulation and prompts the use of computationally less demanding PPE approach [7]. This class of projection methods can eliminate the pressure variable from the momentum equations by applying a curl differential operator to derive the following Poisson equation for pressure in lieu of the divergence-free continuity equation (2.1):

$$\nabla^2 p = 2\left(\frac{\partial u}{\partial x}\frac{\partial v}{\partial y} - \frac{\partial u}{\partial y}\frac{\partial v}{\partial x} - \frac{Q^2}{2}\right) + \left(\frac{1}{Re}\nabla^2 Q - \frac{\mathrm{D}Q}{\mathrm{D}t}\right), \tag{2.3}$$

where $Q = \nabla \cdot \underline{\mathbf{u}}$.

We now justify whether the incompressible Navier–Stokes solutions for $(\underline{\mathbf{u}}, p)$ can be rigorously obtained from Eqs. (2.2) and (2.3). As Eq. (2.1) shows, it is trivial that $Q = 0$ within the differential context. Eq. (2.3) can, thus, be simplified as

$$\nabla^2 p = 2\left(\frac{\partial u}{\partial x}\frac{\partial v}{\partial y} - \frac{\partial u}{\partial y}\frac{\partial v}{\partial x}\right). \tag{2.4}$$

Subtraction of (2.4) from (2.3) leads to the following nonlinear partial differential equation for Q:

$$\frac{1}{Re}\nabla^2 Q - \frac{\mathrm{D}Q}{\mathrm{D}t} - Q^2 = 0. \tag{2.5}$$

As mentioned earlier, the closure initial condition for Eqs. (2.1) and (2.2) is $Q(t = 0) = 0$, which is the trivial solution for Eq. (2.5). In continuous sense, one can rationally replace Eq. (2.1) by Eq. (2.3) or (2.4) in the analysis of incompressible Navier–Stokes equations. At the discrete level, Q is not at all equal to zero because of the indispensable machine and discretization errors. Since Eq. (2.1) serves as the equation for the Lagrangian multiplier, any error that may lead to $Q \neq 0$ is prohibited. This potential drawback in the conventional PPE solution algorithm [8–10] motivated us to discard one of the two momentum equations, say u (or v), and replace it with the divergence-free Eq. (2.1) for the equation v (or u). Within this newly proposed mass-preserving segregated solution framework, the chosen governing equations for $(\underline{\mathbf{u}}, p)$ are as follows:

$$\nabla \cdot \underline{\mathbf{u}} = 0, \tag{2.1}$$

$$\frac{\partial v}{\partial t} + (\underline{\mathbf{u}} \cdot \nabla)v = -\frac{\partial p}{\partial y} + \frac{1}{Re}\nabla^2 v, \tag{2.6}$$

$$\nabla^2 p = 2\left(\frac{\partial u}{\partial x}\frac{\partial v}{\partial y} - \frac{\partial u}{\partial y}\frac{\partial v}{\partial x}\right). \tag{2.4}$$

Employment of Eq. (2.4) is theoretically subjected to the integral boundary condition for p [11]. The computationally difficult integral pressure boundary condition is avoided by applying the following Neumann-type pressure boundary condition [12]:

$$\frac{\partial p}{\partial n} = \left[\frac{1}{Re}\nabla^2\underline{\mathbf{u}} - (\underline{\mathbf{u}}\cdot\nabla)\underline{\mathbf{u}} - \frac{\partial\underline{\mathbf{u}}}{\partial t}\right]\cdot\underline{\mathbf{u}}, \tag{2.7}$$

where $\mathbf{n}$ denotes the unit outward normal vector to the physical boundary.

Now, the convective term in the elliptic–parabolic equation (2.6) is linearized based on the Newton–Raphson method [13–15]. For a product term ST, where S and T are two chosen variables, ST is expanded in Taylor series about its current value and the terms with orders higher than one are neglected. Then the result is as follows [16]:

$$\begin{aligned} S^{n+1}T^{n+1} &= S^nT^n + \left[\frac{\partial}{\partial S}(ST)^n\right](S^{n+1}-S^n) \\ &\quad + \left[\frac{\partial}{\partial T}(ST)^n\right](T^{n+1}-T^n) + \cdots + \text{H.O.T.} \\ &= S^{n+1}T^n + S^nT^{n+1} - S^nT^n + \cdots + \text{H.O.T.} \end{aligned} \tag{2.8}$$

In the following derivation, the superscripts n and $n+1$ denote the variables evaluated at the previous solutions and the most updated iteration (active quantities of the variables), respectively. According to Eq. (2.8), $(uv)_y$ and $(v^2)_y$ are linearized as

$$(uv)_x^{n+1} = u_x^{n+1}v^n + u^{n+1}v_x^n + u_x^nv^{n+1} + u^nv_x^{n+1} - u_x^nv^n - u^nv_x^n, \tag{2.9}$$

$$(v^2)_y^{n+1} = v_y^{n+1}v^n + v^{n+1}v_y^n + v_y^nv^{n+1} + v^nv_y^{n+1} - v_y^nv^n - v^nv_y^n. \tag{2.10}$$

Substituting (2.9) and (2.10) into (2.6), the linearized y-momentum equation can be expressed by the following convection–diffusion–reaction (CDR) equation for v:

$$\begin{aligned} &\frac{\partial v^{n+1}}{\partial t} + (\underline{\mathbf{u}}^n\cdot\nabla)v^{n+1} - \frac{1}{Re}\nabla^2 v^{n+1} + \underline{v_y^nv^{n+1}} \\ &\quad = -p_y^{n+1} + \underline{(\underline{\mathbf{u}}^n\cdot\nabla)v^n - v_x^nu^{n+1}}. \end{aligned} \tag{2.11}$$

By omitting the underlined terms from the above Newton-linearized equation, the conventional coefficient-frozen equation is obtained.

3. Discretization of equations on non-staggered grids

By defining F_j at the grid index j, we get the following equation:

$$\left.\frac{\partial u}{\partial x}\right|_j = \frac{F_j}{h} = -\left.\frac{\partial v}{\partial y}\right|_j, \tag{3.1}$$

where h denotes the uniform grid size. The nodal value for u at j can be implicitly calculated from

$$\begin{aligned} \alpha_2u_{j+1} + \beta_2u_j + \gamma_2u_{j-1} = b_1F_{j+2} + b_2F_{j+1} + b_3F_j \\ + b_4F_{j-1} + b_5F_{j-2}. \end{aligned} \tag{3.2}$$

By expanding $u_{j\pm1}$, $F_{j\pm1}$ and $F_{j\pm2}$ with respect to j in Taylor series, we get

$$u_{j\pm1} = u_j \pm h\frac{\partial u}{\partial x} + \frac{h^2}{2!}\frac{\partial^2u}{\partial x^2} \pm \frac{h^3}{3!}\frac{\partial^3u}{\partial x^3} + \frac{h^4}{4!}\frac{\partial^4u}{\partial x^4} \pm \frac{h^5}{5!}\frac{\partial^5u}{\partial x^5} + \cdots \tag{3.3}$$

$$F_{j\pm1} = F_j \pm h\frac{\partial F}{\partial x} + \frac{h^2}{2!}\frac{\partial^2F}{\partial x^2} \pm \frac{h^3}{3!}\frac{\partial^3F}{\partial x^3} + \frac{h^4}{4!}\frac{\partial^4F}{\partial x^4} \pm \frac{h^5}{5!}\frac{\partial^5F}{\partial x^5} + \cdots \tag{3.4}$$

$$\begin{aligned} F_{j\pm2} &= F_j \pm (2h)\frac{\partial F}{\partial x} + \frac{(2h)^2}{2!}\frac{\partial^2F}{\partial x^2} \pm \frac{(2h)^3}{3!}\frac{\partial^3F}{\partial x^3} + \frac{(2h)^4}{4!}\frac{\partial^4F}{\partial x^4} \\ &\quad \pm \frac{(2h)^5}{5!}\frac{\partial^5F}{\partial x^5} + \cdots \end{aligned} \tag{3.5}$$

By substituting (3.3)–(3.5) into (3.2), the following equation is obtained in lieu of the definition given in (3.1):

$$\begin{aligned} &(\alpha_2+\beta_2+\gamma_2)u_j + (\alpha_2-\gamma_2)h\frac{\partial u}{\partial x} + (\alpha_2+\gamma_2)\frac{h^2}{2!}\frac{\partial^2u}{\partial x^2} \\ &\quad + (\alpha_2-\gamma_2)\frac{h^3}{3!}\frac{\partial^3u}{\partial x^3} + (\alpha_2+\gamma_2)\frac{h^4}{4!}\frac{\partial^4u}{\partial x^4} + (\alpha_2-\gamma_2)\frac{h^5}{5!}\frac{\partial^5u}{\partial x^5} + \cdots \\ &\quad = (b_1+b_2+b_3+b_4+b_5)F_j + (2b_1+b_2-b_4-2b_5)h\frac{\partial F}{\partial x} \\ &\qquad + (4b_1+b_2+b_4+4b_5)\frac{h^2}{2!}\frac{\partial^2F}{\partial x^2} \\ &\qquad + (8b_1+b_2-b_4-8b_5)\frac{h^3}{3!}\frac{\partial^3F}{\partial x^3} \\ &\qquad + (16b_1+b_2+b_4+16b_5)\frac{h^4}{4!}\frac{\partial^4F}{\partial x^4} \\ &\qquad + (32b_1+b_2-b_4-32b_5)\frac{h^5}{5!}\frac{\partial^5F}{\partial x^5} + \cdots \end{aligned} \tag{3.6}$$

Let $\alpha_2+\beta_2+\gamma_2=0$, $\alpha_2-\gamma_2=1$ and $b_1+b_2+b_3+b_4+b_5=1$, $\frac{1}{2!}(\alpha_2+\gamma_2)=(2b_1+b_2-b_4-2b_5)$, $\frac{1}{3!}(\alpha_2-\gamma_2)=\frac{1}{2!}(4b_1+b_2+b_4+4b_5)$, $\frac{1}{4!}(\alpha_2+\gamma_2)=\frac{1}{3!}(8b_1+b_2-b_4-8b_5)$ and $\frac{1}{5!}(\alpha_2-\gamma_2)=\frac{1}{4!}(16b_1+b_2+b_4+16b_5)$. Also, $b_1=0$ and $b_5=0$ are assumed at the left and right points, respectively, to derive the following three-point stencil discretization equations:

$$\begin{aligned} \text{left node}\quad &\frac{19}{30}u_{j+1} + \frac{-4}{15}u_j + \frac{-11}{30}u_{j-1} \\ &= \frac{-1}{90}F_{j+2} + \frac{4}{15}F_{j+1} + \frac{19}{30}F_j + \frac{1}{9}F_{j-1} \end{aligned} \tag{3.7}$$

$$\begin{aligned} \text{center node}\quad &\frac{1}{2}u_{j+1} - \frac{1}{2}u_{j-1} \\ &= \frac{-1}{180}F_{j+2} + \frac{17}{90}F_{j+1} + \frac{19}{30}F_j + \frac{17}{90}F_{j-1} + \frac{-1}{180}F_{j-2} \end{aligned} \tag{3.8}$$

$$\begin{aligned} \text{right node}\quad &\frac{11}{30}u_{j+1} + \frac{4}{15}u_j + \frac{-19}{30}u_{j-1} \\ &= \frac{1}{9}F_{j+1} + \frac{19}{30}F_j + \frac{4}{15}F_{j-1} + \frac{-1}{90}F_{j-2}. \end{aligned} \tag{3.9}$$

By virtue of the modified equation analysis for (3.7)–(3.9), it is easy to show that the above approximations render the fifth order accuracy.

Eq. (3.8) reveals that the void diagonal term can destabilize the matrix equation. To diagonalize the matrix equation, Eqs. (3.7) and (3.9) are shifted towards the left and right by one stencil point, respectively, to get

$$\frac{19}{30}u_{j+2}+\frac{-4}{15}u_{j+1}+\frac{-11}{30}u_j =\frac{-1}{90}F_{j+3}+\frac{4}{15}F_{j+2}+\frac{19}{30}F_{j+1}+\frac{1}{9}F_j, \tag{3.10}$$

$$\frac{11}{30}u_j+\frac{4}{15}u_{j-1}+\frac{-19}{30}u_{j-2} =\frac{1}{9}F_j+\frac{19}{30}F_{j-1}+\frac{4}{15}F_{j-2}+\frac{-1}{90}F_{j-3}. \tag{3.11}$$

By virtue of $w\cdot(3.10)+(1-w)\cdot(3.8)$ and $w\cdot(3.8)+(1-w)\cdot(3.11)$, the following two equations are derived, respectively,

$$\frac{19}{30}u_{j+2}+\frac{7}{30}u_{j+1}+\frac{-11}{30}u_j+\frac{-1}{2}u_{j-1} =\frac{-1}{90}F_{j+3}+\frac{47}{180}F_{j+2}+\frac{37}{45}F_{j+1}+\frac{67}{90}F_j+\frac{17}{90}F_{j-1}+\frac{-1}{180}F_{j-2}, \tag{3.12}$$

$$\frac{1}{2}u_{j+1}+\frac{11}{30}u_j+\frac{-7}{30}u_{j-1}+\frac{-19}{30}u_{j-2} =\frac{-1}{180}F_{j+2}+\frac{17}{90}F_{j+1}+\frac{67}{90}F_j+\frac{37}{45}F_{j-1}+\frac{47}{180}F_{j-2}+\frac{-1}{90}F_{j-3}. \tag{3.13}$$

In what follows, the free parameter w is chosen as $\frac{1}{10}$.

It is well known that use of the staggered approaches for the incompressible flow simulation can effectively suppress the pressure oscillations arising from the even–odd coupling but these approaches can increase the coding complexity. Therefore, in the literature, discretization of differential equations over a domain, where the velocities and pressure are stored at the same point, has been proposed. Approximation of ∇p must be carefully done in the non-staggered mesh system, otherwise, spurious oscillations in the pressure field will be inevitable. The underlying idea of avoiding the even–odd decoupling solutions is to employ p_j while approximating ∇p at an interior node j. Instead of explicitly approximating $\frac{\partial p}{\partial x}$ at node j, its value is obtained implicitly with two additional adjacent values $\frac{\partial p}{\partial x}|_{j\pm1}$. Define F_j as $F_j=h\frac{\partial p}{\partial x}|_j$, where h denotes the uniform mesh size. The method to calculate the nodal value of F is based on the following implicit equation [16,17]:

$$\alpha_1F_{j+1}+\beta_1F_j+\gamma_1F_{j-1}=a_1(p_{j+2}-p_{j+1})+a_2(p_{j+1}-p_j) +a_3(p_j-p_{j-1})+a_4(p_{j-1}-p_{j-2}). \tag{3.14}$$

The above seven coefficients are obtained by expanding $F_{j\pm1}$ in Taylor series with respect to F_j, and $p_{j\pm1}$ and $p_{j\pm2}$ with respect to p_j. This is followed by substituting these expansion equations into Eq. (3.14) and by employing the definition for F_j to derive a simultaneous set of algebraic equations. It is legitimate to set $\alpha_1=\gamma_1$ due to the elliptic nature of p_j. Then, the other coefficients are determined as $\alpha_1=\frac{1}{5}$, $\beta_1=\frac{3}{5}$, $a_1=\frac{1}{60}$, $a_2=\frac{29}{60}$, $a_3=\frac{29}{60}$, and $a_4=\frac{1}{60}$. For example, the equation for F_j at a node immediately adjacent to the right boundary point, is derived from Eq. (3.14) at $\alpha_1=a_1=a_2=0$.

4. CDR scheme and its fundamental studies

4.1. Five-point CDR scheme

In view of Eq. (2.11), the following model equation for $\phi(\phi=v)$ is considered:

$$a\frac{\partial\phi}{\partial x}+b\frac{\partial\phi}{\partial y}-k\nabla^2\phi+c\phi=f. \tag{4.1}$$

To eliminate the convective instability and to retain the prediction accuracy in the approximation of the above CDR equation, the following general solution to Eq. (4.1) is employed:

$$\phi(x,y)=A_1\mathrm{e}^{\lambda_1x}+A_2\mathrm{e}^{\lambda_2x}+A_3\mathrm{e}^{\lambda_3y}+A_4\mathrm{e}^{\lambda_4y}+\frac{f}{c}, \tag{4.2}$$

where $A_1\sim A_4$ are the four constants. By substituting Eq. (4.2) into Eq. (4.1), $\lambda_1\sim\lambda_4$ are derived as

$$\lambda_{1,2}=\frac{a\pm\sqrt{a^2+4ck}}{2k}\quad\text{and}\quad\lambda_{3,4}=\frac{b\pm\sqrt{b^2+4ck}}{2k}. \tag{4.3}$$

The discrete equation at an interior node (i,j) is assumed to take the following five-point stencil form:

$$\left(-\frac{a}{2h}-\frac{m}{h^2}+\frac{c}{12}\right)\phi_{i-1,j}+\left(\frac{a}{2h}-\frac{m}{h^2}+\frac{c}{12}\right)\phi_{i+1,j} +4\left(\frac{m}{h^2}+\frac{2c}{12}\right)\phi_{i,j}+\left(-\frac{b}{2h}-\frac{m}{h^2}+\frac{c}{12}\right)\phi_{i,j-1} +\left(\frac{b}{2h}-\frac{m}{h^2}+\frac{c}{12}\right)\phi_{i,j+1}=f_{i,j}. \tag{4.4}$$

Then, by substituting the exact solutions $\phi_{i,j}=A_1\mathrm{e}^{\lambda_1x_i}+A_2\mathrm{e}^{\lambda_2x_i}+A_3\mathrm{e}^{\lambda_3y_j}+A_4\mathrm{e}^{\lambda_4y_j}+\frac{f}{c}$, $\phi_{i\pm1,j}=A_1\mathrm{e}^{\pm\lambda_1h}\mathrm{e}^{\lambda_1x_i}+A_2\mathrm{e}^{\pm\lambda_2h}\mathrm{e}^{\lambda_2x_i}+A_3\mathrm{e}^{\lambda_3y_j}+A_4\mathrm{e}^{\lambda_4y_j}+\frac{f}{c}$ and $\phi_{i,j\pm1}=A_1\mathrm{e}^{\lambda_1x_i}+A_2\mathrm{e}^{\lambda_2x_i}+A_3\mathrm{e}^{\pm\lambda_3h}\mathrm{e}^{\lambda_3y_j}+A_4\mathrm{e}^{\pm\lambda_4h}\mathrm{e}^{\lambda_4y_j}+\frac{f}{c}$ into Eq. (4.4), m is derived as

$$m=\left[\frac{ah}{2}\sinh\overline{\lambda_1}\cosh\overline{\lambda_2}+\frac{bh}{2}\sinh\overline{\lambda_3}\cosh\overline{\lambda_4} +\frac{ch^2}{12}(\cosh\overline{\lambda_1}\cosh\overline{\lambda_2}+\cosh\overline{\lambda_3}\cosh\overline{\lambda_4}+10)\right] \Big/(\cosh\overline{\lambda_1}\cosh\overline{\lambda_2}+\cosh\overline{\lambda_3}\cosh\overline{\lambda_4}-2), \tag{4.5}$$

where $(\overline{\lambda_1},\overline{\lambda_2})=(\frac{ah}{2k},\sqrt{(\frac{ah}{2k})^2+\frac{ch^2}{k}})$ and $(\overline{\lambda_3},\overline{\lambda_4})=(\frac{bh}{2k},\sqrt{(\frac{bh}{2k})^2+\frac{ch^2}{k}})$.

In view of the banded matrix with the components given in Eq. (4.4), it is possible to get $a_{ij}\leqslant0$ with $i\neq j$ and $|a_{ii}|\geqslant\sum|a_{ij}|(i\leqslant j)$. Under these circumstances, the matrix equation is irreducible and also diagonally dominant. The matrix of this type is called as M-matrix. Since the inverse matrix of $\{a_{i,j}\}$ (or $\underline{\underline{\mathbf{A}}}^{-1}$) is greater than zero, namely,

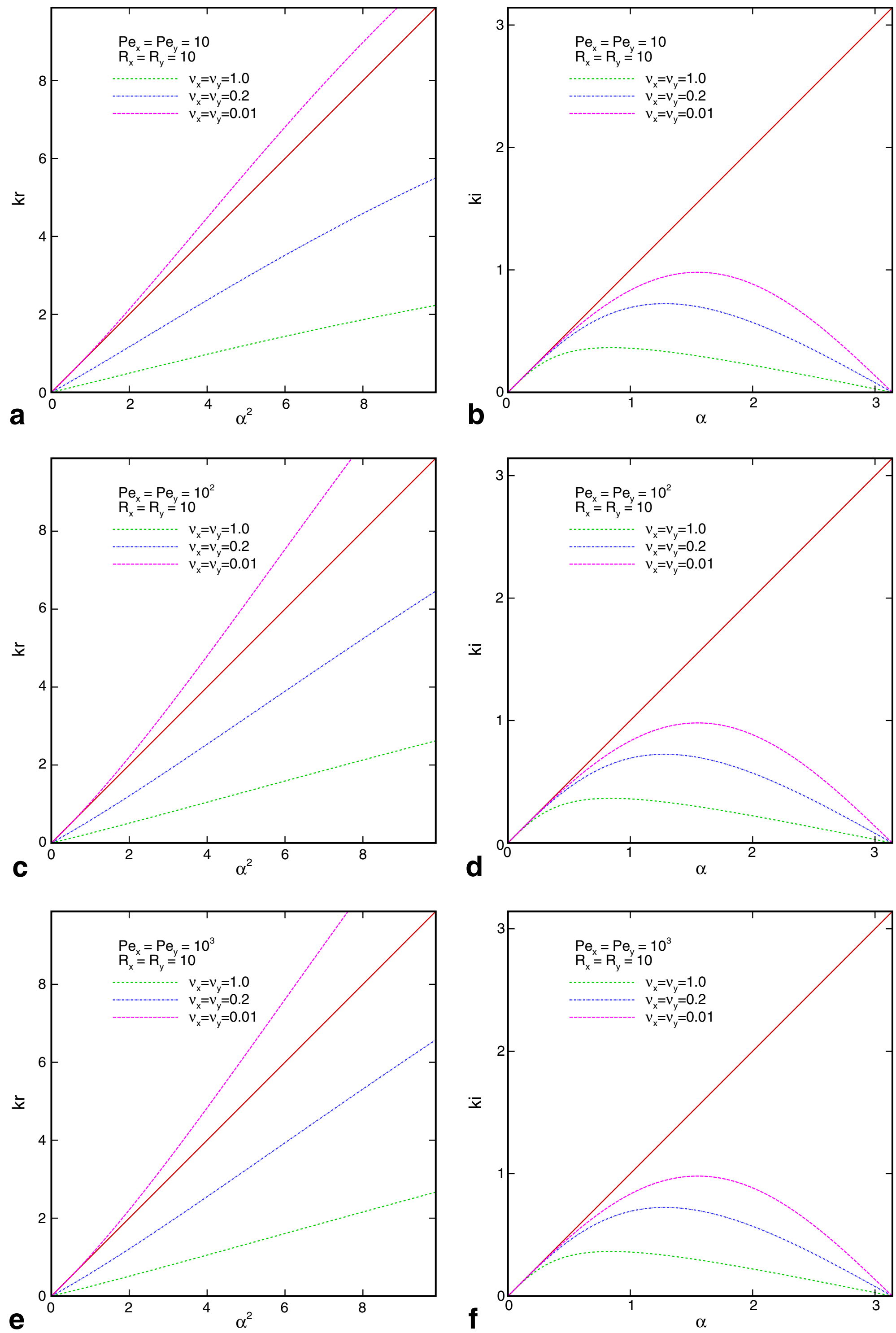

Fig. 1. Plots of k_r and k_i against α^2 and α, respectively, at $R_x = R_y = 10$, Pe and v, (a,b) $Pe = 10$; (c,d) $Pe = 10^2$; (e,f) $Pe = 10^3$. Note that α is the modified wave-number.

$\underline{\underline{\mathbf{A}}}^{-1} > 0$, the solutions computed from the M-matrix equation are unconditionally monotonic. By following the M-matrix theory [18], it is appropriate to employ the proposed scheme to resolve any possible sharp profile of ϕ in the flow.

Throughout the present paper, the second derivative terms for the velocities are approximated by the compact scheme [16,17]. For example, consider ϕ_{xx} at j. Calculation of $\phi_{xx}|_j$ starts by assuming $\phi_{xx}|_j = \frac{S_j}{h^2}$, then value of S_j is implicitly computed from

$$h^2(\alpha_3 S_{j+1} + \beta_3 S_j + \gamma_3 S_{j-1}) = c_1\phi_{j+2} + c_2\phi_{j+1} + c_3\phi_j + c_4\phi_{j-1} + c_4\phi_{j-2}. \tag{4.6}$$

Expanding $S_{j\pm 1}$ with respect to S_j and $\phi_{j\pm 1}$, $\phi_{j\pm 2}$ with respect to ϕ_j in Taylor series and then substituting them into the expression for S_j, $(\alpha_3, \beta_3, \gamma_3, c_1, c_2, c_3, c_4, c_5) = \left(1, \frac{11}{2}, 1, \frac{3}{8}, 6, -\frac{51}{4}, 6, \frac{3}{8}\right)$ are obtained from the eight algebraic equations for α_3, β_3, γ_3, c_1, c_2, c_3, c_4 and c_5.

Note that the above CDR scheme breaks down at the limiting conditions of $u_i = 0$ and $c_3 = 0$. Discretization of Eq. (2.4) should be treated differently. One way to accurately approximate p_{xx} and p_{yy} is to employ Eq. (4.6) at $\alpha_3 = \gamma_3 = 0$. Other free parameters can be determined using the same method described earlier. The resulting discrete equation for $\nabla^2 p$ at an interior point (i,j) is given by

$$\nabla^2 p|_{i,j} = (p_{i+1,j+1} + p_{i-1,j+1} + p_{i+1,j-1} + p_{i-1,j-1}) - 20p_{i,j} + 4(p_{i+1,j} + p_{i-1,j} + p_{i,j+1} + p_{i,j-1}). \quad (4.7)$$

The quality of approximating Eq. (2.4) depends highly on the first derivative terms shown in the right hand side of that equation. Depending on the sign of u, the value of u_x at the left boundary is obtained by assuming $\alpha_3 = \gamma_3 = 0$ in Eq. (4.6). The remaining coefficients are determined as $\beta_3 = 1$, $c_1 = -\frac{1}{12}$, $c_2 = \frac{4}{3}$, $c_3 = -\frac{5}{2}$, $c_4 = \frac{4}{3}$ and $c_5 = -\frac{1}{12}$.

4.2. Dispersion and Fourier analysis of the CDR discretization scheme

With the initial condition $\phi(x, y, t = 0) = \exp\,[\mathrm{i}k_m(x + y)]$, Eq. (4.1) analyzed at $f = 0$ has the following exact solution:

$$\phi(x, y, t) = \exp[-(2kk_m^2 + c)t] \exp\{\mathrm{i}k_m[(x + y) - (a + b)t]\}, \quad (4.8)$$

where k_m denotes the wave-number. Choosing h $(\equiv \Delta x = \Delta y)$ as the mesh size and Δt as the time step, the discrete equation for (4.1) is as follows:

$$B_1\phi_{i-1,j}^{n+1} + B_2\phi_{i+1,j}^{n+1} + B_3\phi_{i,j}^{n+1} + B_4\phi_{i,j-1}^{n+1} + B_5\phi_{i,j+1}^{n+1} = \phi_{i,j}^n, \quad (4.9)$$

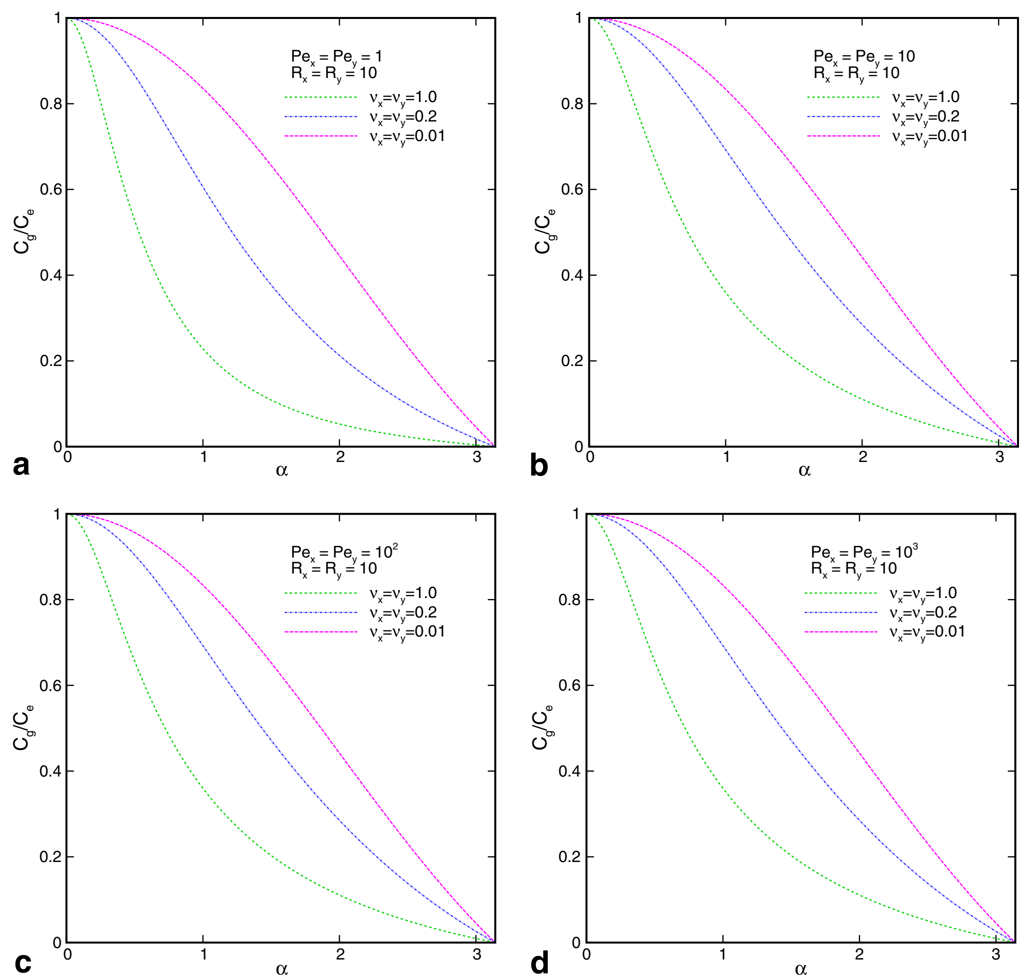

Fig. 2. Plots of the group velocity ratio $\frac{C_g}{C_e}$ against the modified wave-number α at $R_x = R_y = 10$, Pe and v, (a) $Pe = 1$; (b) $Pe = 10$; (c) $Pe = 10^2$; (d) $Pe = 10^3$.

where

$$B_{1,2} = -\overline{m} \mp \frac{v_x}{2} + \frac{v_x R_x + 2}{24}, \tag{4.10}$$

$$B_3 = 4\left(\overline{m} + \frac{v_x R_x + v_y R_y + 2}{12}\right), \tag{4.11}$$

$$B_{4,5} = -\overline{m} \mp \frac{v_y}{2} + \frac{v_y R_y + 2}{24}. \tag{4.12}$$

In the above equations, $(v_x, v_y) = (\frac{a\Delta t}{h}, \frac{b\Delta t}{h})$. By defining $(Pe_x, Pe_y) = (\frac{ah}{k}, \frac{bh}{k})$ and $(R_x, R_y) = (\frac{ch}{a}, \frac{ch}{b})$, $\overline{m}$ shown in Eqs. (4.10)–(4.12) is expressed as

$$\overline{m} = \left[\frac{v_x}{2}\sinh\overline{\lambda_1}^*\cosh\overline{\lambda_2}^* + \frac{v_y}{2}\sinh\overline{\lambda_3}^*\cosh\overline{\lambda_4}^* + \frac{v_x R_x + v_y R_y + 2}{24} \times (\cosh\overline{\lambda_1}^*\cosh\overline{\lambda_2}^* + \cosh\overline{\lambda_3}^*\cosh\overline{\lambda_4}^* + 10)\right] \Big/ (\cosh\overline{\lambda_1}^*\cosh\overline{\lambda_2}^* + \cosh\overline{\lambda_3}^*\cosh\overline{\lambda_4}^* - 2), \tag{4.13}$$

where $(\overline{\lambda_1}^*, \overline{\lambda_2}^*) = \left(\frac{Pe_x}{2}, \sqrt{(\frac{Pe_x}{2})^2 + \frac{Pe_x}{v_x}}\right)$ and $(\overline{\lambda_3}^*, \overline{\lambda_4}^*) = \left(\frac{Pe_y}{2}, \sqrt{(\frac{Pe_y}{2})^2 + \frac{Pe_y}{v_y}}\right)$.

Owing to the indispensable amplitude and phase errors, the exact solution to the five-point stencil equation (4.1) is assumed to take the following form:

$$\phi(x,y,t) = \exp\left[-t(2kk_m^2 + c)\frac{k_r}{\alpha^2}t\right] \times \exp\left\{ik_m\left[(x+y) - (a+b)\frac{k_i}{\alpha}t\right]\right\}. \tag{4.14}$$

The modified wave-number given in the above equation is denoted as $\alpha = k_m h$. Dispersion analysis involves the substitution of $\phi_{i,j}$, $\phi_{i\pm1,j}$ and $\phi_{i,j\pm1}$, which are obtained from Eq. (4.14), into Eq. (4.1). After some algebra k_r and k_i, which are responsible for the respective amplitude and phase errors, are derived as

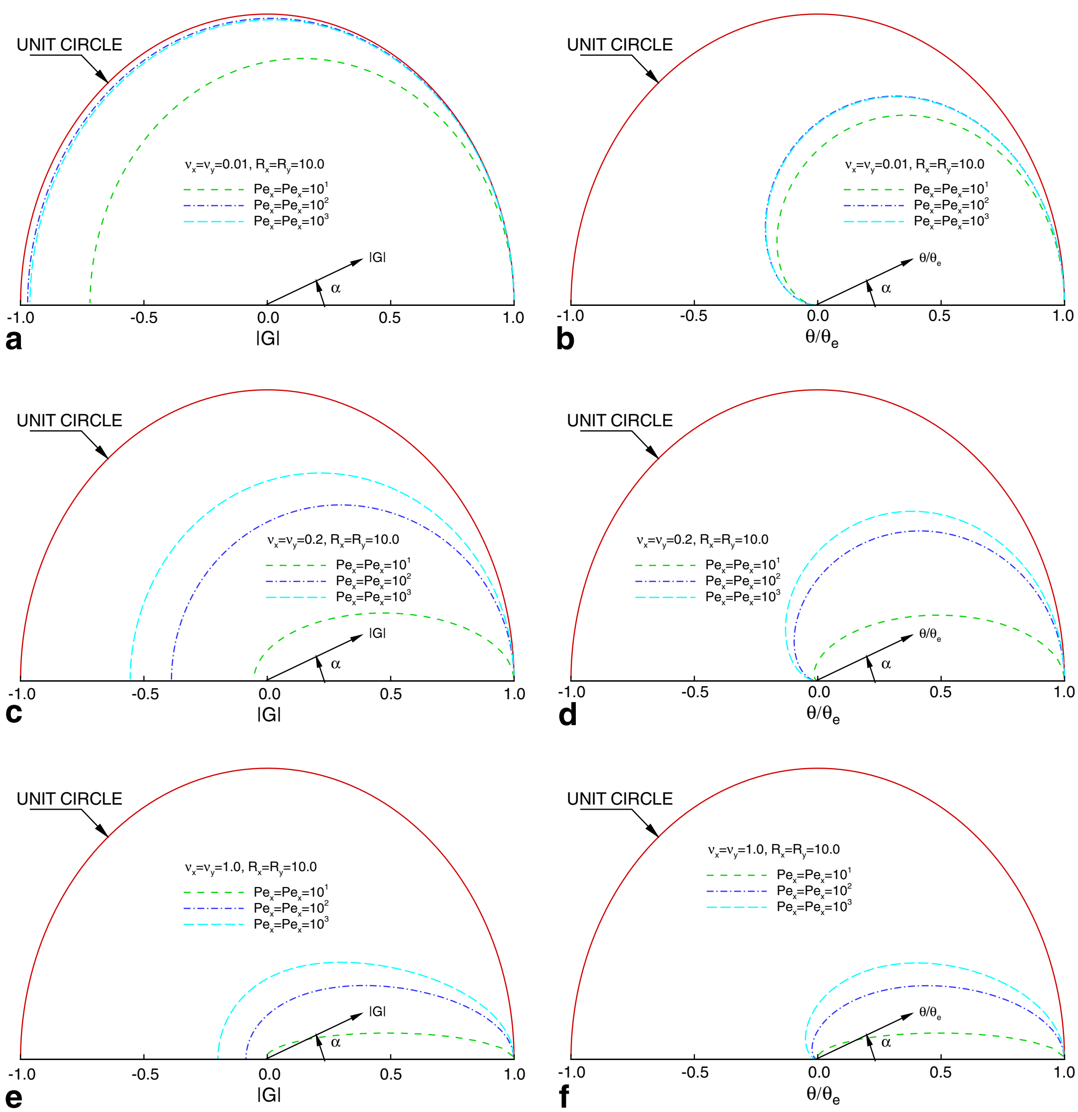

Fig. 3. Plots of the amplification factor $|G|$ in (a), (c), (e) and the phase angle ratio $\frac{\theta}{\theta_e}$ in (b), (d), (f) against the modified wave-number α at $R_x = R_y = 10$, Pe and v, (a,b) $v_x = v_y = 0.01$; (c,d) $v_x = v_y = 0.2$; (e,f) $v_x = v_y = 1.0$.

$$k_r = -\frac{p}{\frac{v_x}{Pe_x} + \frac{v_y}{Pe_y} + \frac{v_x R_x + v_y R_y}{2\alpha^2}}, \tag{4.15}$$

$$k_i = -\frac{q}{v_x + v_y}, \tag{4.16}$$

where $(v_x, v_y) = (\frac{a\Delta t}{h}, \frac{b\Delta t}{h})$, $(Pe_x, Pe_y) = (\frac{ah}{k}, \frac{bh}{k})$, $(R_x, R_y) = (\frac{ch}{a}, \frac{ch}{b})$ and

$$q = \tan^{-1}\left[\frac{(B_1 - B_2 + B_4 - B_5)\sin\alpha}{(B_1 + B_2 + B_4 + B_5)\cos\alpha + B_3}\right], \tag{4.17}$$

$$p = \ln\left\{\frac{1}{\cos q[(B_1 + B_2 + B_4 + B_5)\cos\alpha + B_3] + \sin q[(B_1 - B_2 + B_4 - B_5)\sin\alpha]}\right\}. \tag{4.18}$$

In Fig. 1, the plots for k_r and k_i against (Pe_x, Pe_y) and (v_x, v_y) (at the fixed values of R_x and R_y) enlighten that k_i agrees perfectly with α in the small modified wave-number range. It is observed that the larger the modified wave-number, the less satisfactory is the predicted numerical phase. In contrast to k_i, the amplitude error is not well resolved even in the small wave-number range. Also, in Fig. 2 the numerical group velocity $C_g(\equiv \frac{dW}{dk_m})$ is plotted, where $W(\equiv k_m \frac{k_i}{\alpha}\underline{\mathbf{u}})$ is obtained from the dispersion equation. It can be seen that C_g has a magnitude smaller than the analytical propagation speed. The proposed scheme is, thus, of the phase-lagging type.

The Fourier (or von Neumann) stability analysis [19,20] is also conducted in the present study. Let $\alpha = \frac{2\pi m}{2L}h$ $(m = 0, 1, 2, \ldots, M)$, h be the grid size and $2L$ be the period of fundamental frequency $(m = 1)$. Then the amplification factor $G(\equiv \phi_{i,j}^{n+1}/\phi_{i,j}^{n})$ is derived as

$$G = \frac{A - \mathrm{i}B}{A^2 + B^2}, \tag{4.19}$$

where

$$A = \frac{4\overline{m}}{h^2}(1 - \cos\alpha) + \frac{1}{6}(v_x R_x + v_y R_y + 2)(\cos\alpha + 2), \tag{4.20}$$

$$B = (v_x + v_y)\sin\alpha. \tag{4.21}$$

The proposed implicit scheme is unconditionally stable in the sense that $|G| \leqslant 1$.

The amplification factor shown in (4.19) is rewritten as $G = |G|e^{\mathrm{i}\theta}$, where θ is the phase angle:

$$\theta = \tan^{-1}\left|\frac{\mathrm{Im}(G)}{\mathrm{Re}(G)}\right| = \tan^{-1}\left(\frac{-B}{A}\right). \tag{4.22}$$

The exact phase angle is derived as $\theta_e = -k_m h(v_x + v_y)$, where $k_m(\equiv \frac{2\pi m}{2L},\ m = 0, 1, 2, \ldots, M)$ denotes the wave number and $(v_x, v_y) = (\frac{u\Delta t}{h}, \frac{v\Delta t}{h})$ are the Courant numbers (h be the grid size). Using the exact phase angle, the relative phase shift error over an arbitrary time step is given by

$$\frac{\theta}{\theta_e} = \frac{\tan^{-1}(-B/A)}{-\alpha(v_x + v_y)}. \tag{4.23}$$

In Figs. 3 and 4, θ/θ_e against α, (v_x, v_y), (Pe_x, Pe_y) and (R_x, R_y) are plotted. When the relative phase error exceeds the value one at the specified values of v and Pe, the numerical wave has a speed greater than the exact wave speed. The resulting error is called the phase-leading error. Conversely, the error is called the lagging phase error. As the figure shows, the proposed scheme is classified as phase-lagging scheme since it has a phase-lagging error irrespective of the values of v, Pe and R.

5. Numerical results

5.1. Validation of the proposed linearization method

To verify the proposed Newton linearization method, the following nonlinear convection–diffusion equation for u is investigated in $0 \leqslant x, y \leqslant 1$:

$$u\frac{\partial u}{\partial x} + b\frac{\partial u}{\partial y} - k\nabla^2 u = f(x, y). \tag{5.1}$$

Under the circumstances of $k = x^2$, $b = y$ and $f(x, y) = 2x^3(y^4 - x)$, the solution to Eq. (5.1) was exactly derived as $u(x, y) = x^2y^2$. Good agreement between the simulated and exact solutions is seen in Table 1. Assessment is made on the proposed linearization model and the standard relaxation method given by $\underline{\mathbf{u}}^{\text{new}} = \gamma\underline{\mathbf{u}}^{\text{new}} + (1 - \gamma)\underline{\mathbf{u}}^{\text{old}}$, where $0 \leqslant \gamma \leqslant 1$. As Fig. 5 shows, the number of nonlinear iterations has been considerably reduced in view of the number of iterations needed for the cases considered at $\gamma = 0.2$, 0.4, 0.6 and 0.8. The tolerance, defined as $\left[\frac{1}{N}\sum(\underline{\mathbf{u}}^{\text{new}} - \underline{\mathbf{u}}^{\text{old}})^2\right]^{1/2}$, set for each calculation is 10^{-15}, where N denotes the number of nodal points.

5.2. Validation of the proposed Navier–Stokes method

To verify the proposed Navier–Stokes methodology, the problem amenable to the analytic solution is considered. Within the two-dimensional domain $\Omega = [0,1]\times[0,1]$, the Navier–Stokes equations are solved at $Re = 10^3$ along with the following analytical boundary velocities [21]:

$$u(x, y) = (x\sin(2xy) + y\cos(2xy))\exp(x^2 - y^2), \tag{5.2}$$

$$v(x, y) = (x\cos(2xy) - y\sin(2xy))\exp(x^2 - y^2). \tag{5.3}$$

The exact pressure is derived as

$$p(x, y) = c_1 - \frac{1}{2}(x^2 + y^2)\exp[2(x^2 - y^2)]. \tag{5.4}$$

In Fig. 6 and Table 2, the rate of convergence for $\phi(=\underline{\mathbf{u}}, p)$ is calculated according to the solutions obtained at the successively refined domains of uniform grid sizes h_1 and h_2

$$C = \frac{\log(E_2/E_1)}{\log(h_2/h_1)}. \tag{5.5}$$

Table 1
The computed error norms and the corresponding rates of convergence C

Mesh points	$\|u - u_{\text{exact}}\|$	C
6×6	6.772×10^{-8}	
11×11	1.897×10^{-8}	1.835
21×21	5.001×10^{-9}	1.923
31×31	2.261×10^{-9}	1.957
41×41	1.282×10^{-9}	1.970

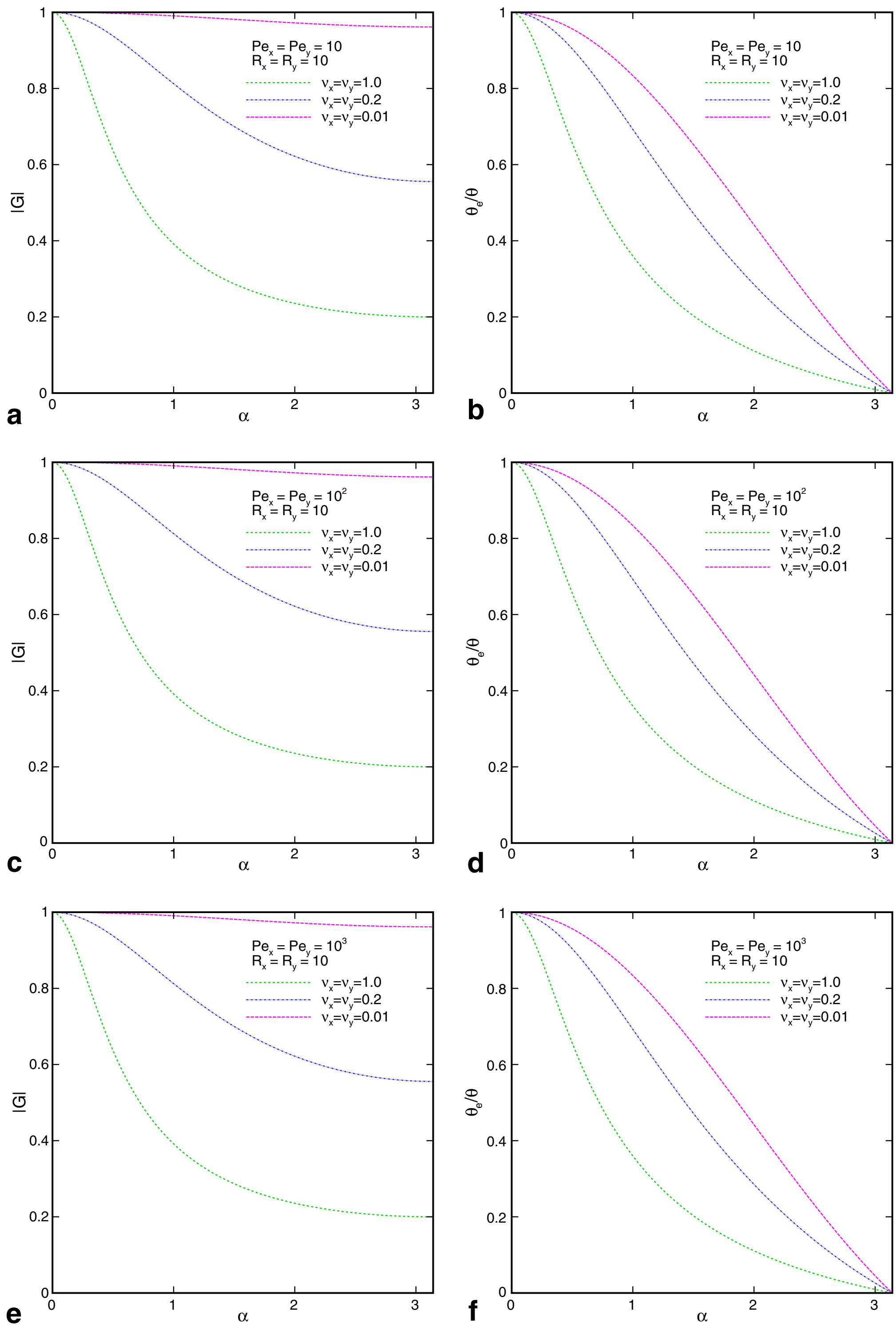

Fig. 4. Plots of the amplification factor $|G|$ in (a), (c), (e) and the phase angle ratio $\frac{\theta}{\theta_e}$ in (b), (d), (f) against the modified wave-number α at $R_x = R_y = 10$, Pe and ν, (a,b) $Pe = 10$; (c,d) $Pe = 10^2$; (e,f) $Pe = 10^3$.

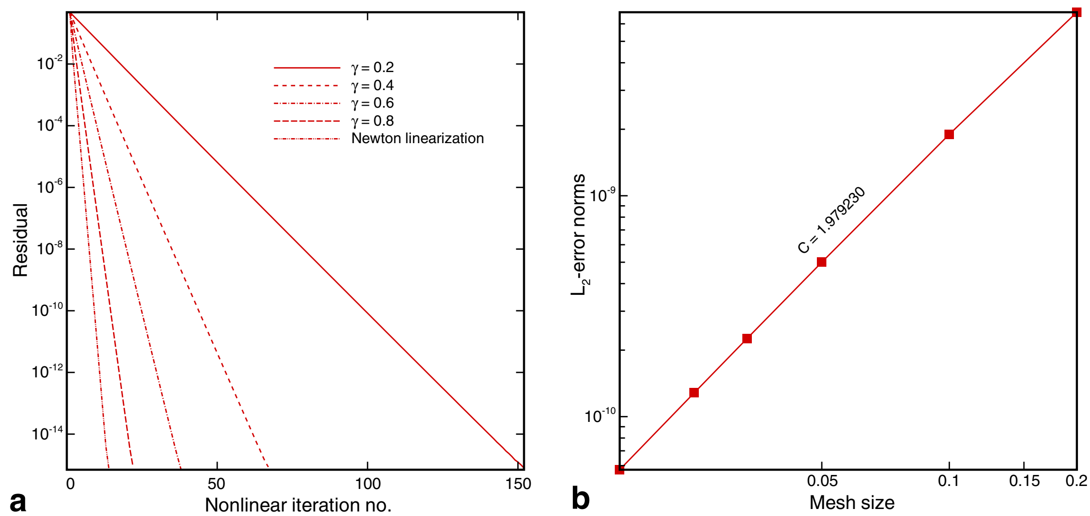

Fig. 5. (a) Comparison of the convergent histories, with the initially guessed value $u = 0.5$, using the present and the conventional PPE methods to solve the nonlinear advection–diffusion equation (5.1); (b) the plot of L_2-error norms against the mesh sizes for showing the rate of convergence C.

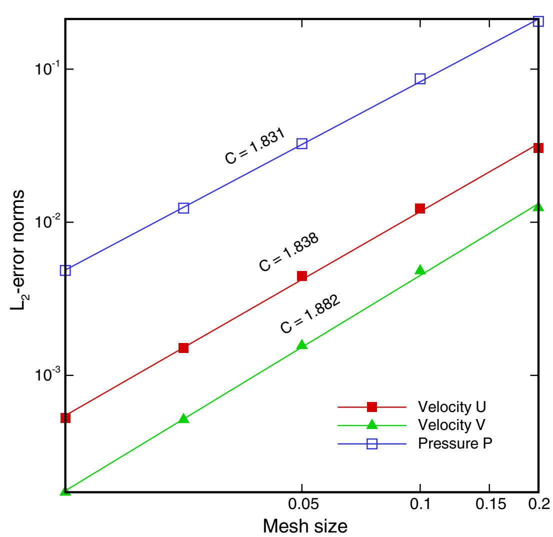

Fig. 6. The rates of convergence C for the two-dimensional Navier–Stokes problem with the solutions given in Eqs. (5.2)–(5.4).

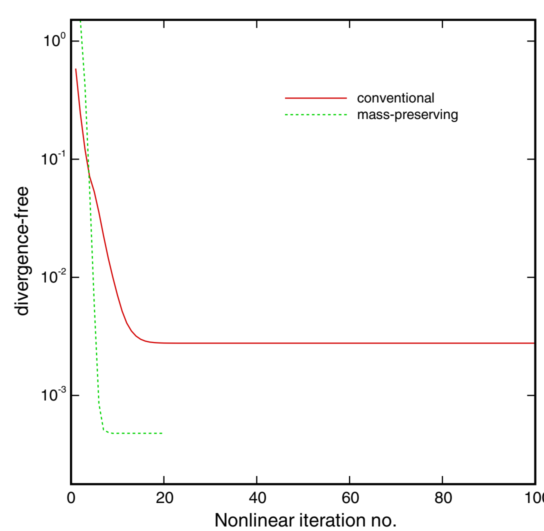

Fig. 7. Assessment of the degree of mass-preserving for the two PPE formulations by virtue of the simulated magnitude of $\nabla \cdot \underline{\mathbf{u}}$.

Table 2
The computed error norms and the corresponding rates of convergence C for u, v and p

Mesh points	$\Vert u - u_{\text{exact}} \Vert$	C	$\Vert v - v_{\text{exact}} \Vert$	C	$\Vert p - p_{\text{exact}} \Vert$	C
6×6	1.374×10^{-3}		1.651×10^{-3}		2.404×10^{-3}	
11×11	3.757×10^{-4}	1.870	3.145×10^{-4}	2.392	6.085×10^{-4}	1.982
21×21	8.817×10^{-5}	2.091	7.653×10^{-5}	2.039	1.421×10^{-4}	2.098
41×41	1.863×10^{-5}	2.242	1.361×10^{-5}	2.491	3.446×10^{-5}	2.044

The error E is measured in the L_2-norm form as

$$E = \left[\sum_{i=1}^{N} (\phi_{ij} - \Phi_{ij})^2 \delta x_i \delta y_j \right]^{1/2}. \tag{5.6}$$

In the above equation, $\phi = \phi(x_i, y_j)$ denotes the nodal exact solution at a point (i,j) and Φ_{ij} is the corresponding computed solutions. The L_2-norms of $\nabla \cdot \underline{\mathbf{u}}$ are calculated and plotted in Fig. 7 against the nonlinear iteration to show that the divergence-free condition is indeed achieved. For the sake of completeness, reduction of the residuals for $\underline{\mathbf{u}}$ and p is also plotted against the nonlinear iteration numbers in Fig. 8. The simulated velocity vector and pressure contours are also plotted in Fig. 9.

Encouraged by the above success in validating the steady-state problems, the transient Navier–Stokes equations are solved in a unit square for the problem having the following exact solutions:

$$u(x, y, t) = 1 + 2\cos[2\pi(x - t)]\sin[2\pi(y - t)]\mathrm{e}^{-8\pi^2 \nu t}, \tag{5.7}$$

$$v(x, y, t) = 1 - 2\sin[2\pi(x - t)]\cos[2\pi(y - t)]\mathrm{e}^{-8\pi^2 \nu t}, \tag{5.8}$$

$$p(x, y, t) = c_2 - \{\cos[4\pi(x - t)] + \cos[4\pi(y - t)]\}\mathrm{e}^{-16\pi^2 \nu t}. \tag{5.9}$$

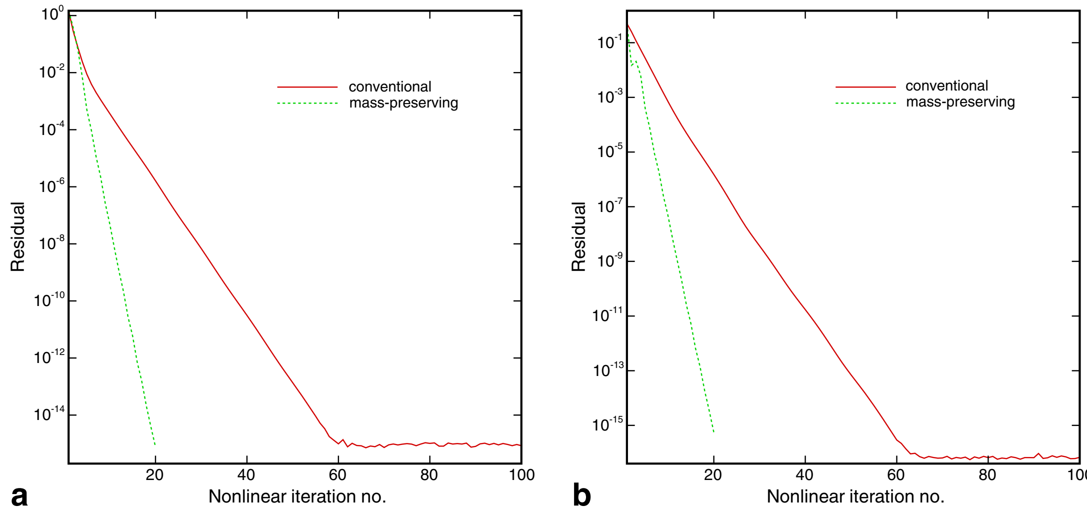

Fig. 8. The plots of residual reduction for $\underline{\mathbf{u}} = (u, v)$ and p based on the two-dimensional Navier–Stokes problem given in Eqs. (5.2)–(5.4): (a) velocity and (b) pressure.

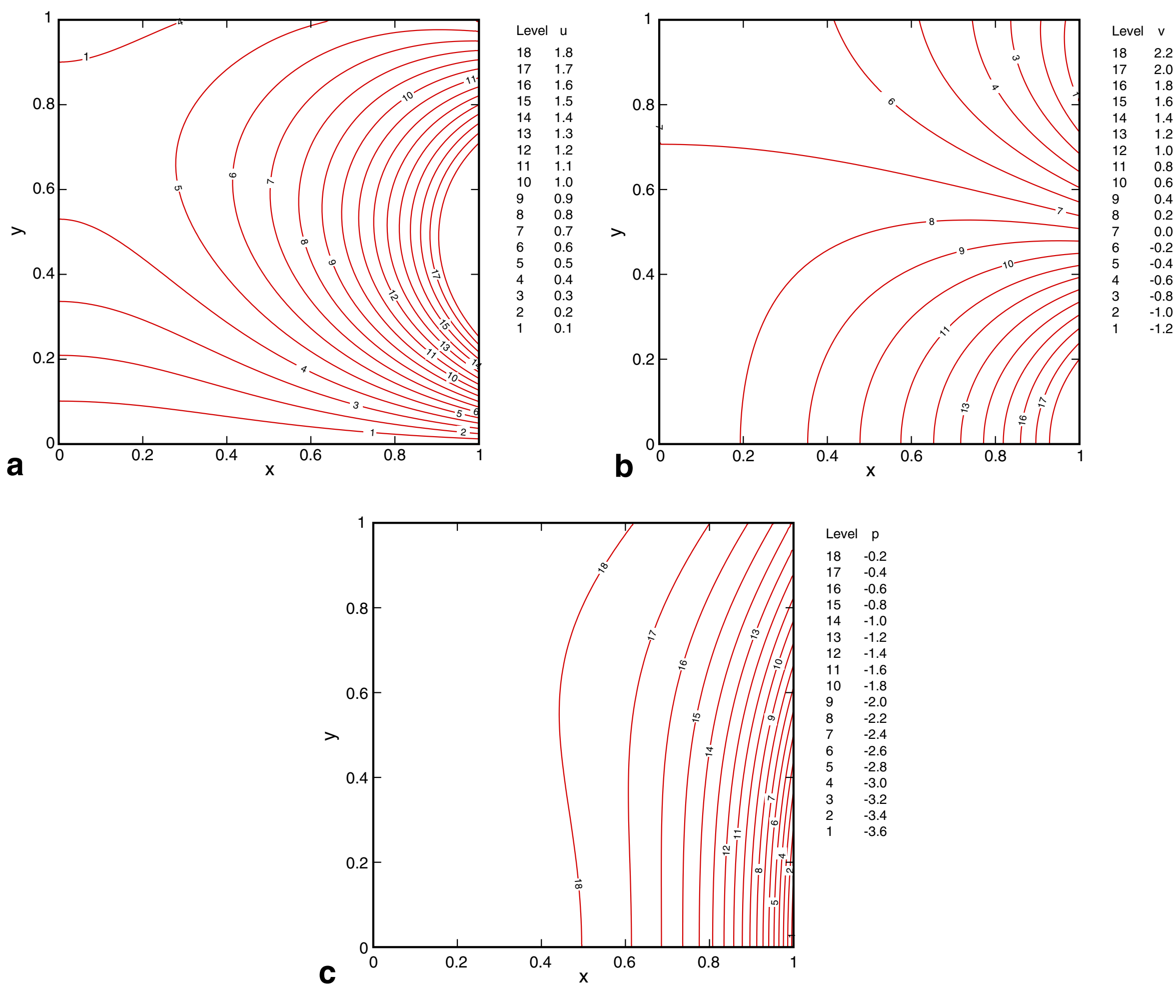

Fig. 9. The simulated solution contours at $Re = 10^3$ ((—) present solution; (---) exact solution) given in (5.2)–(5.4): (a) velocity u, (b) velocity v, (c) pressure.

All the solutions are obtained in $0 \leqslant x,\ y \leqslant 1$. In Fig. 10, the simulated contours are plotted for u, v and p at $t = 1$, $\nu = 10^{-3}$, $\Delta x = \Delta y = \frac{1}{20}$ and $\Delta t = 10^{-2}$. Computations are also performed over a range of four mesh sizes $h = \frac{1}{2^n}$, where $n = 4, 5, 6, 7$, at $\nu = 10^{-3}$ and $\Delta t = 10^{-2}$ for the sake of completeness. The proposed method is validated based on the L_2-norm errors plotted in Fig. 11.

5.3. Lid-driven cavity flow problem

The Navier–Stokes fluid flow in a square cavity, which is driven by a constant upper lid velocity u_{lid}, is studied. With L as the characteristic length and u_{lid} as the characteristic velocity, the Reynolds number under investigation is chosen as 5000. We continuously refine the mesh and plot the grid-independent mid-plane velocity profiles $u(0.5, y)$ and $v(x, 0.5)$ in Fig. 12. For the sake of comparison, the steady-state benchmark solutions of Ghia [22] and Erturk [23] are also plotted in the same figure. Besides the good

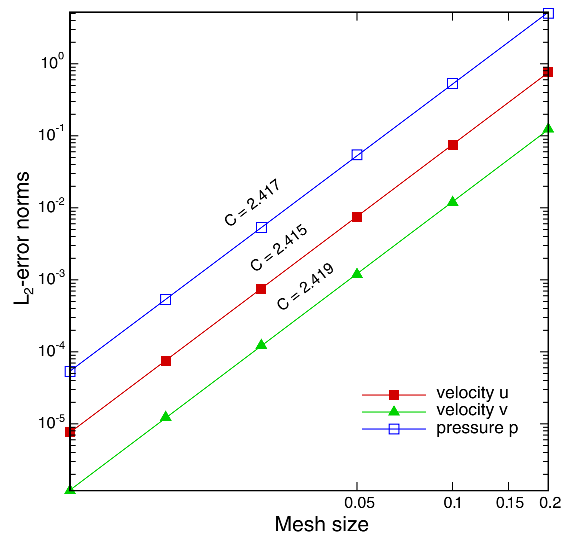

Fig. 11. The rates of convergence C for the two-dimensional Navier–Stokes problem with solutions given in Eqs. (5.7)–(5.9).

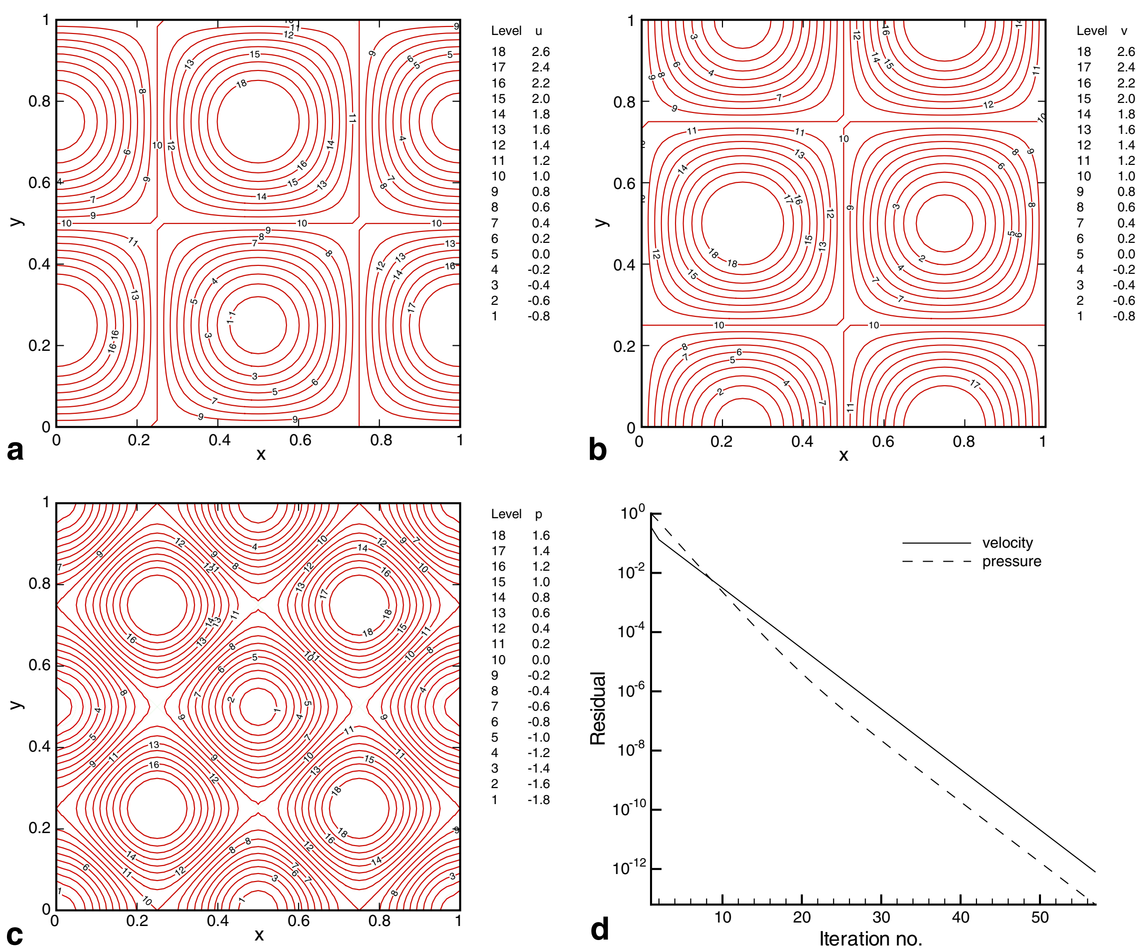

Fig. 10. The simulated solution contours at $\nu = 10^{-3}$ and $t = 1.0$ ((—) present solution; (- - -) exact solution) given in (5.7)–(5.9): (a) velocity u, (b) velocity v, (c) pressure, (d) convergent history for the case with 64×64 mesh points.

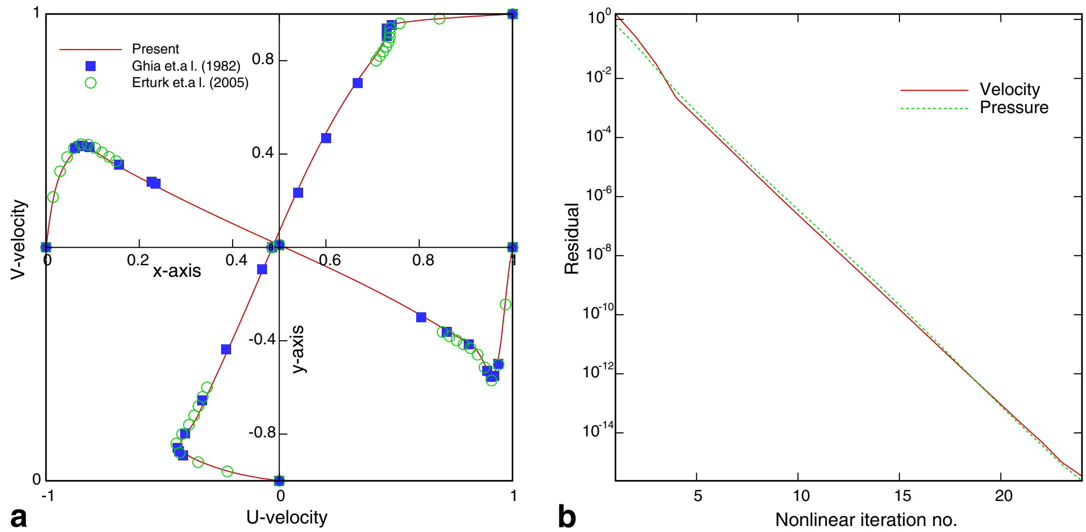

Fig. 12. (a) Comparison of the simulated and Ghia's velocity profiles for $u(x,0.5)$ and $v(0.5,y)$ at $Re = 5000$; (b) The plots of the residual reduction for $(|\underline{\mathbf{u}}|, p)$ against the nonlinear iteration numbers.

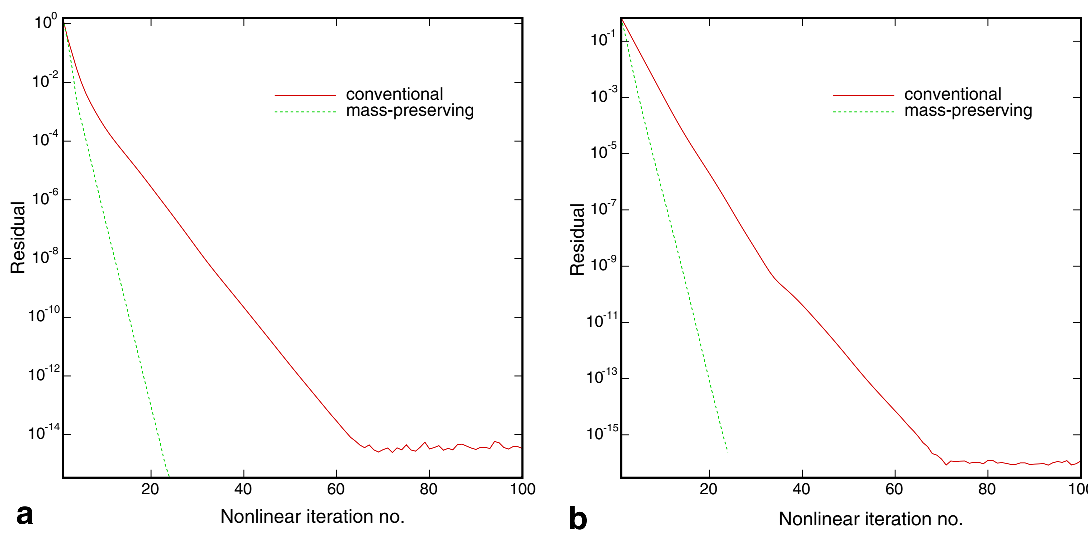

Fig. 13. The plots of the residual reduction for $(\underline{\mathbf{u}}, p)$ in the investigation of the lid-driven cavity flow problem: (a) velocity and (b) pressure.

agreement between the present and previous solutions, much improved convergent histories are also seen in Fig. 13. The applicability of the proposed scheme is, thus, confirmed.

6. Conclusions

The proposed mass-preserving segregated Navier–Stokes method for solving the incompressible flow equations has two main features: one is its ability to circumvent the spurious pressure oscillations on the non-staggered grid and the other is the transformation of the convection–diffusion differential equation into its convection–diffusion–reaction counterpart. Both the dissipative and dispersive natures of the proposed five-point stencil CDR scheme have been rigorously revealed. Good agreement between the simulated and analytical solutions is demonstrated for the two test problems. Also, the spatial rate of convergence is observed to be very high.

Acknowledgements

Part of the work was supported by the National Science Council of the Republic of China under Grant NSC 94-2611-E-002-021. The first author would like to thank the excellent facility provided by Shanghai Institute of Applied Mathematics and Mechanics in the course of his sabbatical leave in Shanghai University.

References

[1] S.V. Patankar, A calculation procedure for two-dimensional elliptic situations, Numer. Heat Transfer 4 (1981) 409–425.

[2] S.V. Patankar, D.B. Spalding, A calculation procedure for heat, mass and momentum transfer in three-dimensional parabolic flows, Int. J. Heat Mass Transfer 15 (1972) 1787–1806.

[3] J. Papageorgakopoulos, G. Arampatzis, D. Assimacopoulos, N.C. Markatos, Enhancement of the momentum interpolation method on non-staggered grids, Int. J. Numer. Meth. Fluids 33 (2000) 1–12.

[4] C.M. Rhie, W.L. Chow, Numerical study of the turbulent flow past an aerofoil with trailing edge separation, AIAA J. 21 (1983) 1525–1532.

[5] S.V. Patankar, Numerical Heat Transfer and Fluid Flow, Hemisphere, New York, 1980.

[6] F.H. Harlow, J.E. Welch, Numerical calculation of time-dependent viscous incompressible flow of fluid with free surface, Phys. Fluids 8 (12) (1965) 2182–2189.

[7] P.M. Gresho, R.L. Sani, On pressure boundary conditions for the incompressible Navier–Stokes equations, Int. J. Numer. Meth. Fluids 7 (1987) 1111–1145.

[8] S. Abdallah, Numerical solutions for the incompressible Navier–Stokes equations in primitive variables using a non-staggered grid, I, II, J. Comput. Phys. 70 (1987) 183–202.

[9] F. Sotiropoulos, S. Abdallah, A primitive variable method for the solution of three-dimensional incompressible viscous flows, J. Comput. Phys. 103 (1992) 336–349.

[10] L. Fuchs, H.S. Zhao, Solution of three-dimensional viscous incompressible flows by a multi-grid method, Int. J. Numer. Meth. Fluids 4 (1984) 539–555.

[11] L. Quartapelle, M. Napolitano, Integral conditions for the pressure in the computation of incompressible viscous flows, J. Comput. Phys. 62 (1986) 340–348.

[12] Tony W.H. Sheu, M.M.T. Wang, S.F. Tsai, Pressure boundary conditions for a segregated approach to solving incompressible Navier–Stokes equations, Numer. Heat Transfer, Part B: Fundamentals 34 (4) (1998) 457–467.

[13] R.S. Dembo, S.C. Eisenstat, T. Steihaug, Inexact Newton methods, SIAM J. Numer. Anal. 19 (1982) 400–408.

[14] S.C. Eisenstat, H.F. Walker, Globally convergent inexact Newton methods, SIAM J. Optim. 4 (1994) 393–422.

[15] S.C. Eisenstat, H.F. Walker, Choosing the Newton method, SIAM J. Sci. Comput. 17 (1996) 16–32.

[16] Tony W.H. Sheu, R.K. Lin, Newton linearization on the incompressible Navier–Stokes equations, Int. J. Numer. Meth. Fluids 44 (2004) 297–312.

[17] Tony W.H. Sheu, R.K. Lin, An incompressible Navier–Stokes model implemented on non-staggered grids, Numer. Heat Transfer, Part B: Fundamentals 44 (2003) 277–294.

[18] T. Meis, U. Marcowitz, Numerical solution of partial differential equations, Applied Mathematical Science, vol. 22, Springer-Verlag, 1981.

[19] R.D. Richtmyer, K.W. Morton, Difference Methods for Initial Value Problems, Interscience Publishers, Wiley & Sons, 1967.

[20] J. von Neumann, R.D. Richtmyer, A method for the numerical calculation on hydrodynamic shock, J. Appl. Phys. 21 (1950) 232–237.

[21] Tony W.H. Sheu, S.F. Tsai, Morten M.T. Wang, A Petrov–Galerkin formulation for incompressible Navier–Stokes flows at high Reynolds numbers, Int. J. Comput. Fluid Dyn. 5 (1995) 213–230.

[22] U. Ghia, K.N. Ghia, C.T. Shin, High-*Re* solutions for incompressible flow using the Navier–Stokes equations and a multigrid method, J. Comput. Phys. 48 (1982) 387–411.

[23] E. Erturk, T.C. Corke, C. Gökçöls, Numerical solution of 2-D steady incompressible driven cavity flow at high Reynolds numbers, Int. J. Numer. Meth. Fluids 48 (2005) 747–774.